PAPER

Check for updates

Investigation on the structural, optical, photoluminescence and electric properties of a semiconductor material [Br(CH₂)₂N(CH₃)₃]₂SnBr₆

Amal Elghoul,[a] Bochra Ben Salah,[b] Fadhel Hajlaoui, [ID] *[a] Karim Karoui, [ID] [cd] Nathalie Audebrand,[e] Thierry Roisnel,[e] Erika Kozma, [ID] [f] Chiara Botta[f] and Nabil Zouari[a]

A new low-dimensional hybrid tin(IV) halides, $[Br(CH_2)_2N(CH_3)_3]_2SnBr_6$, was synthesized *via* slow evaporation from acidic aqueous solution under ambient conditions. Single-crystal X-ray diffraction reveals that the compound crystallizes in the orthorhombic space group *Pbca*, featuring discrete $[SnBr_6]^{2-}$ octahedra spatially isolated and electrostatically stabilized by $[Br(CH_2)_2N(CH_3)_3]^+$ cations. The crystal packing is reinforced through a network of C−H···Br hydrogen bonds and halogen···halogen contacts, forming a 0D supramolecular framework. Infrared spectroscopy confirms the existence of characteristic vibrational modes from organic molecule. Furthermore, the thermal behavior studied by (TGA−DSC) indicates good thermal stability up to 430 K. Optical absorption studies yield a direct optical band gap of 3 eV and an indirect gap of 2.54 eV, consistent with semiconducting behavior. Under UV excitation, the compound exhibits blue photoluminescence centered at 434 nm, attributed to excitonic recombination confined within the $[SnBr_6]^{2-}$ units. Impedance spectroscopy further reveals thermally activated conduction, following non-overlapping small polaron tunneling and correlated barrier hopping models. These findings suggest that $[Br(CH_2)_2N(CH_3)_3]_2SnBr_6$ is a structurally robust, lead-free semiconductor with blue emission, making it a promising candidate for environmentally benign optoelectronic devices such as LEDs and photonic components.

Introduction

Since the early 2000s, hybrid organic–inorganic halide perovskites have emerged as key materials for high-performance optoelectronic applications, owing to their structural flexibility and outstanding electronic properties. Following the pioneering work of Kojima *et al.* on MAPbI₃ in solar cells,[1] these materials rapidly expanded into photovoltaics, LEDs, photodetectors, and lasers.[2–7] Perovskites, defined by the ABX₃ structure, consist of $[BX_6]^{4-}$ octahedra that can form 3D corner-sharing frameworks or reduced-dimensional (2D, 1D, 0D) architectures,[8–10] allowing precise control of exciton binding energy, band gap, charge

mobility, and stability.[11] Despite these advances, Pb-based perovskites such as MAPbI₃ and FAPbBr₃ suffer from toxicity and instability.[12–15] Tin-based halides (Sn²⁺) were proposed as alternatives due to their chemical similarity to Pb²⁺,[16] and early studies on CH₃NH₃SnI₃ and FASnI₃ confirmed their photovoltaic potential but also revealed rapid oxidation of Sn²⁺ to Sn⁴⁺, compromising stability.[17–19] This limitation has motivated research into tin(IV)-based systems, where fully oxidized Sn⁴⁺ ions form chemically robust $[SnX_6]^{2-}$ octahedra encapsulated by organic cations, yielding stable zero-dimensional (0D) hybrids.[20–23] These materials display excellent thermal and chemical stability and exhibit enhanced quantum confinement effects that promote strong excitonic emission, particularly in the blue-to-green spectral range. For example, the 0D hybrid $[C_4N_2H_{14}Br]_4SnBr_6$ exhibits strong yellow luminescence at ~360 nm.[24] Substitution at the organic cation site has proven highly effective for band gap tuning and photoluminescence enhancement: [(R)-3-hydroxyquinuclidinium]₂SnCl₆ introduces chirality, induces dielectric switching near 330 K, and presents a wide band gap of 4.11 eV.[25] Furthermore, both the halide anion and the organic cation play a key role in controlling the photophysical behavior of 0D tin-based hybrids. Notably, $(C_4N_2H_{14}Br)_4[SnBr_6]$ and $(C_4N_2H_{14}I)_4[SnI_6]$ exhibit intense yellow and orange photoluminescence under UV excitation, with quantum yields reaching

[a] Laboratoire Physico-chimie de l'Etat Solide, Département de Chimie, Faculté des Sciences de Sfax, Université de Sfax, B.P. 1171, 3000 Sfax, Tunisia. E-mail: fadhelh83@yahoo.fr

[b] Laboratory of Medicinal and Environmental Chemistry, Higher Institute of Biotechnology of Sfax, University of Sfax, 3018 Sfax, Tunisia

[c] Laboratoire des caractérisations spectroscopiques et optique des matériaux, Faculté des Sciences de Sfax, Université de Sfax, B.P. 1171, 3000 Sfax, Tunisia

[d] GREMAN UMR 7347-CNRS, CEA, INSACVL, University of Tours, Blois, France

[e] Univ Rennes, CNRS, INSA Rennes, ISCR (Institut des Sciences Chimiques de Rennes) – UMR 6226, F-35000 Rennes, France

[f] Istituto di Scienze e Tecnologie Chimiche "G. Natta" (SCITEC), CNR, Via G. A. Corti 12, 20133 Milano, Italy

~95% and ~75%, respectively.[26] These materials also display large Stokes shifts (215 nm and 118 nm), attributed to strong exciton–phonon coupling and excited-state relaxation. Such findings emphasize that even small variations in halide composition or organic framework can substantially impact emission efficiency, spectral position, and Stokes behavior. [26] Similarly, halogen substitution within organic cations, such as replacing hydrogen with fluorine in $[C_3H_7FN]_3[SnCl_6]Cl$, leads to order–disorder transitions, preserved ferroelectricity, and multiple phase changes at 293, 391, and 403 K.[27] Mixed-halide systems, where multiple halides coexist in the tin coordination sphere, have also emerged as an effective design strategy. Such compositional tuning allows for photostable band gap modulation and significantly influences photoluminescence intensity.[28,29] A pertinent example is $[Cl–(CH_2)_2–NH_3]_2SnBr_{5.65}Cl_{0.35}$, which demonstrates strong blue emission and a reduced band gap of 2.94 eV compared to its chloride-rich analogue.[30] Additionally, halogen-functionalized ammonium derivatives, such as 2-chloroethylammonium or 2-bromoethyltrimethylammonium, enhance intermolecular interactions through halogen and hydrogen bonding networks. These design principles were exemplified in the work of Sui *et al.*, who synthesized $[BrCH_2-CH_2N(CH_3)_3]_2[CdBr_4]$, a 0D hybrid displaying ferroelectric and switchable dielectric transitions near 342 K and 390 K.[31] Their findings highlight how the incorporation of halogen atoms into the organic framework not only affects packing and symmetry but also enables multifunctional properties, including ferroelectricity and spontaneous polarization. Motivated by these advances, the present work focuses on the synthesis and comprehensive characterization of a new 0D lead-free tin halide hybrid, $[Br(CH_2)_2N(CH_3)_3]_2SnBr_6$. This compound, synthesized *via* slow evaporation in acidic media, incorporates (2-bromoethyl) trimethylammonium cations and isolated $[SnBr_6]^{2-}$ anions within an orthorhombic lattice. Detailed investigations by X-ray diffraction, optical absorption, photoluminescence spectroscopy, electrical impedance spectroscopy, and thermal analysis reveal a direct band gap of 3 eV and blue emission at 434 nm, demonstrating its potential for optoelectronic applications such as light-emitting devices.

Experimental section

Synthetic procedures

All chemicals and solvents used in this synthesis were obtained from commercial suppliers and utilized without any additional purification. Deionized water served as the solvent medium throughout the procedure.

Synthesis of $[Br(CH_2)_2N(CH_3)_3]_2SnBr_6$. The compound was obtained through a slow evaporation process carried out at room temperature. To a solution of (2-bromoethyl)trimethylammonium bromide (0.346 g, 2 mmol) in 15 mL of hydrobromic acid, tin(II) bromide ($SnBr_2$, 0.278 g, 1 mmol) was added under continuous stirring. The mixture was stirred until a clear yellow solution was obtained. This solution was then allowed to evaporate slowly at room temperature. After several days, yellow crystals in the form of block were formed and collected for analysis.

Infrared spectroscopy

The formation of the compound $[Br(CH_2)_2N(CH_3)_3]_2SnBr_6$ was confirmed by IR spectroscopy performed at room temperature using a KBr pellet. As shown in Fig. S1, the spectrum recorded in the 400–4000 cm^{-1} range exhibits characteristic absorption bands. Peaks observed between 672 and 1275 cm^{-1} were assigned to the stretching vibrations of C–N and C–Br bonds. Bands at 1443 and 1480 cm^{-1} correspond to the bending vibrations of methyl C–H groups, while sharp absorptions at 2984 and 3025 cm^{-1} were attributed to the stretching vibrations of methylene (CH_2) C–H bonds. These spectral features are consistent with the structural components of the organic cation and support the successful synthesis of the hybrid halide compound. The band assignments are in agreement with literature data for similar hybrid halide compounds.[31]

Single-crystal X-ray diffraction

Single-crystal X-ray diffraction analysis of $[Br(CH_2)_2N(CH_3)_3]_2SnBr_6$ was performed at 150 K using a Bruker D8 VENTURE diffractometer (CDIFX/ISCR) equipped with a micro-focus Mo-Kα radiation source ($\lambda = 0.71073$ Å) and a CMOS-PHOTON70 detector. Crystal structure has been described in orthorhombic symmetry with *Pbca* space group. The structure was solved using SHELX-T program[32] and refined by full matrix least-squares routines against F^2 using SHELX-L program[33] through the WinGX program suite.[34] Hydrogen atoms were placed in geometrically idealized positions and refined using a riding model (HFIX). Structural illustrations were generated with Diamond software.[35] Crystallographic details and refinement parameters are provided in Table S1, with selected bond lengths and angles listed in Table S2. Complete atomic coordinates and anisotropic displacement parameters are available in the corresponding CIF file. CCDC number 2474595.

Thermal analysis

The thermogravimetric Analysis (TGA) were performed using a Setaram SETSYS 16/18 instrument in the temperature range of 300–700 K with a ramp rate of 5 K min^{-1}.

The thermal behavior of the compound was examined using Differential Scanning Calorimetry (DSC) with a NETZSCH DSC 200 F3 analyzer. Powdered samples (~10 mg) were placed in platinum crucibles, while alumina (Al_2O_3) was used as the reference material. The measurements were conducted under a nitrogen flow, applying heating and cooling rates of 5 K min^{-1}, across a temperature range from 290 to 450 K.

UV-visible absorption spectroscopy

Room-temperature UV-Vis absorption spectra were acquired using Lambda 900 PerkinElmer spectrophotometer operating in transmission mode in the spectral range from 200 to 850 nm.

Photoluminescence spectroscopy

Photoluminescence (PL) spectra were recorded at ambient temperature using a NanoLog composed by a iH320 spectrograph equipped with a Synapse QExtra charge-coupled device by

exciting with a monochromated 450 W Xe lamp. All spectra were corrected for instrument response. Time-resolved TCSPC measurements are obtained with PPD-850 single photon detector module and Delta Time serie DD-300 Delta Diode and analysed with the instrument Software DAS6. PL QY were measured with a home-made integrating sphere according to the procedure reported elsewhere.[36]

Electrical characterization and impedance spectroscopy

Impedance measurements were performed on disk-shaped pellets (8 mm diameter, ~1.3 mm thickness) using a SOLAR-TRON SI 1260 impedance/gain-phase analyzer, interfaced with a dielectric test unit. The real (Z') and imaginary (Z'') components of the impedance were recorded over a frequency range of 1 Hz to 1 MHz and a temperature range of 303–403 K. Copper electrodes (8 mm diameter) were deposited on both sides of the pellets to ensure good electrical contact.
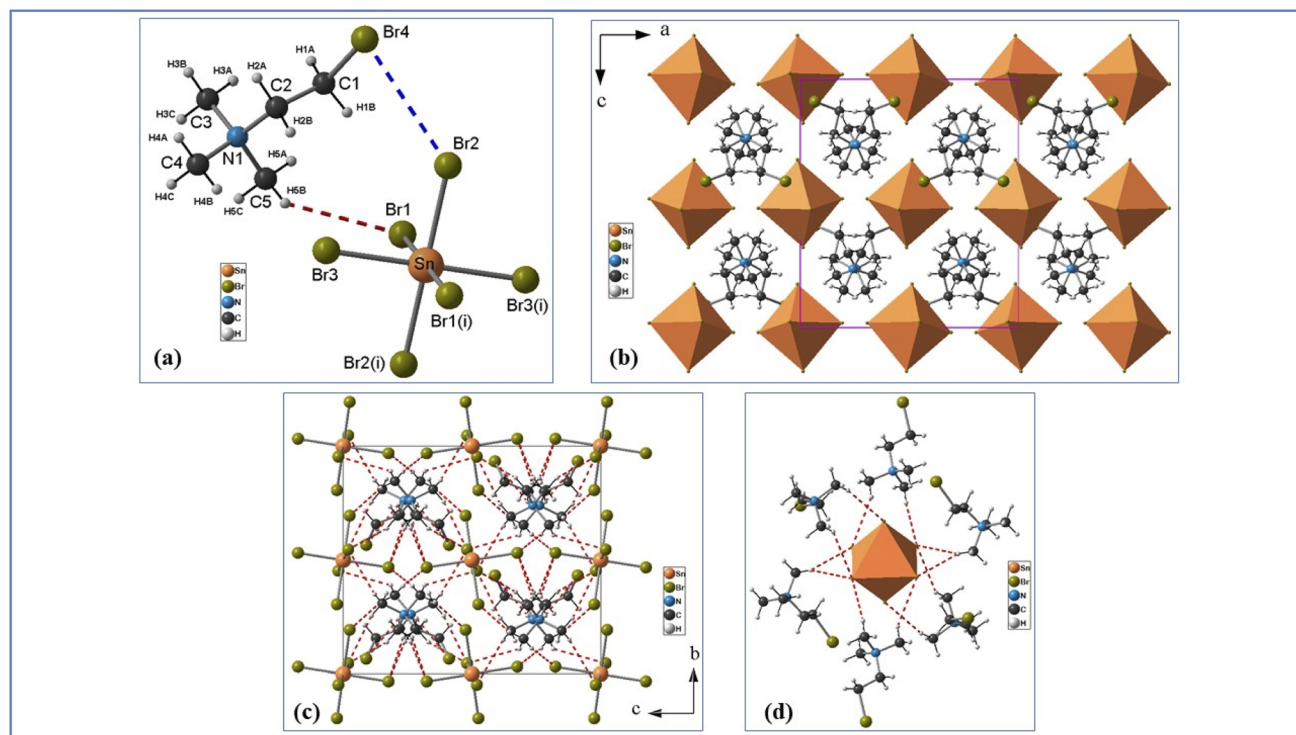
Results and discussion

Structural investigations

The compound was synthesized *via* slow evaporation of an aqueous solution containing tin(IV) bromide, hydrobromic acid, and (2-bromoethyl)trimethylammonium bromide. It crystallizes in the orthorhombic system, space group *Pbca*, with the unit cell parameters: $a = 12.792$ (2) Å, $b = 12.973$ (2) Å, $c = 14.605$ (2) Å, $V = 2423.7$ (6) Å^3 and $Z = 4$ (Table S1). The asymmetric unit of the title compound, $[Br(CH_2)_2N(CH_3)_3]_2SnBr_6$, consists of one organic $[Br(CH_2)_2N(CH_3)_3]^+$ cation and one half-anion (Fig. 1(a)). The $[SnBr_6]^{2-}$ anion is located on an inversion center and forms a quasi-regular octahedral arrangement. Structural cohesion is maintained through a network of C–H⋯Br hydrogen bonds and halogen⋯halogen interactions, forming a zero-dimensional (0D) hybrid framework (Fig. 1(b) and (c)).

A projection of the crystal structure along the *a*- and *b*-axes reveals a 0D architecture formed by alternating layers of isolated $[SnBr_6]^{2-}$ octahedra and $[Br(CH_2)_2N(CH_3)_3]^+$ organic chains (Fig. 1(b) and (c)). This type of arrangement is similar to that found in related hybrid halostannates.[27] Within the inorganic substructure, the Sn(IV) center is coordinated by six bromide ions, forming slightly distorted octahedra with Sn–Br bond lengths ranging from 2.5587 (5) to 2.6156 (5) Å. The *cis* and *trans* Br–Sn–Br angles fall within the ranges 89.112 (11)°–90.888 (11)° and equal to 180.0°, respectively, which are consistent with values observed in related hybrid tin halide compounds.[37] Each $[SnBr_6]^{2-}$ octahedron is surrounded by four $[Br(CH_2)_2N(CH_3)_3]^+$ cations *via* mono-, and bidentate C–H⋯Br hydrogen bonding (Fig. 1(d)), contributing to the cohesion of the supramolecular network (Fig. 1(d)).

The organic moieties exhibit N–C, C–C, and C–Br bond lengths ranging from 1.489 (4)–1.511 (4) Å, 1.502 (4) Å, and 1.943 (3) Å, respectively. Bond angles for C–N–C, C–C–Br, and N–C–C lie between 107.1 (2)°–111.3 (2)°, 108.8 (2)° and 114.4 (2)°,

Fig. 1 (a) Molecular structure of $[Br(CH_2)_2N(CH_3)_3]_2SnBr_6$. Hydrogen bonds are represented by red dotted lines; halogen bonds are shown as blue dash line. Symmetry codes: (i) $-x + 1$, $-y + 1$, $-z + 1$. (b) Projection of the structure along the *b*-axis. (c) Projection of the $[Br(CH_2)_2$-$N(CH_3)_3]_2SnBr_6$ structure in the (b and c) plane. C–H⋯Br hydrogen bonds are shown in red line (d) neighbouring (2-bromoethyl)tri-methylammonium cations in the environment of $[SnBr_6]^{2-}$.

respectively (Table S3). An extended network of hydrogen bonds links the organic cations to the $[SnBr_6]^{2-}$ anions, with C–H⋯Br distances ranging from 3.669 (3) to 3.995 (3) Å, and the C–H⋯Br bond angles vary between 118 and 168° reinforcing the supramolecular structure (see Fig. 1(c) and Table S4). In addition, the halogen bonds between ions were observed in the structure. Indeed, the short intermolecular Br⋯Br contact of 3.817(3) Å between Br4 atom and Br2 atom leads to the formation of type II halogen bonds ($\theta 1 = 129.1(5)°$, $\theta 2 = 85.31(5)°$), which is shown in Fig. 1(a) as a blue dashed line. The bonds length and angle values of halogen interactions were found to be comparable to literature data obtained with other similar hybrid compounds such as $[Br(CH_2)_2N(CH_3)_3]_2M^{II}Br_4$; ($M^{II} = Cu^{2+}$ or Cd^{2+}).[31]

Thermal decomposition

This study evaluates the thermal stability of $[Br(CH_2)_2N(CH_3)_3]_2SnBr_6$ using thermogravimetric analysis (TGA), and differential scanning calorimetry (DSC). The TGA curve displays two main weight loss events (Fig. S2). The first, occurring between 300 and 320 K, corresponds to a 5% mass loss and is attributed to the removal of water. A second weight loss of ∼54.35% is observed between ∼480 and 550 K, likely due to the decomposition of the organic cations together with the bromide is removed to support the charge neutrality and corresponds to the formation of $SnBr_4$ (theoretical weight loss, 52.98%). This decomposition behavior is consistent with that reported for structurally related hybrid stannate halides.[38] The DSC thermogram of the $[Br(CH_2)_2N(CH_3)_3]_2SnBr_6$ compound was recorded in the temperature range from 290 K to 450 K, as shown in Fig. S3. The thermal analysis reveals no evidence of phase transitions within this temperature range, indicating the structural stability of the compound in these thermal conditions. These results have been confirmed by complex impedance measurements with the electrical conductivity. A weak endothermic peak is observed near 323 K, which is attributed to

the release of adsorbed surface water. This anomaly does not correspond to any structural change in the crystal lattice and is instead related to the mild hygroscopic nature of the material.

UV-visible spectroscopy and band gap analysis

The optical absorption properties of $[Br(CH_2)_2N(CH_3)_3]_2SnBr_6$ was investigated at room temperature using UV-visible spectroscopy. Fig. 2 shows the absorption spectrum recorded in the wavelength range of 200–700 nm. The absorption band is observed at approximately 350 nm. This absorption is attributed to band-to-band electronic transitions, in which electrons are excited from the valence band primarily composed of Br 4p orbitals to the conduction band formed by the Sn 5s and 5p orbitals in the $[SnBr_6]^{2-}$ octahedra.

The optical band gap energy was further analyzed using Tauc's method, based on the classical relation:[39]

$$(\alpha h\nu)^n = B (h\nu - E_g)$$

With α the optical absorbance, $h\nu$ the photon energy, B a constant, then E_g the optical band gap, $n = 2$ or $1/2$ for direct and indirect allowed transition, respectively. The plot of $(\alpha h\nu)^2$ and $(\alpha h\nu)^{0.5}$ as a function of photon energy ($h\nu$) are presented in the inset of Fig. 2. Extrapolation of the linear portions of these plots to the photon energy axis, where $(\alpha h\nu)^n = 0$ (towards x-axis) provides estimates of the optical band gap energies. The direct band gap was determined to be 3.0 eV, while the indirect band gap was found to be 2.54 eV. These values are consistent with those reported for other 0D hybrid tin(IV) halide perovskites.[27,36,40] The optical bandgaps of these compounds (between 2.5 and 2.8 eV) are related to their molecular structure. This comparison reinforces the classification of $[Br(CH_2)_2N(CH_3)_3]_2SnBr_6$ as a band-gap semiconductor, highlighting its potential for use in light-harvesting and optoelectronic devices.

Photoluminescence properties

The photoluminescence (PL) properties of $[Br(CH_2)_2N(CH_3)_3]_2SnBr_6$ were investigated at room temperature in air to evaluate its emission characteristics. Measurements were conducted on both powder and cast film samples, as shown in Fig. 3 and 4. The PL spectra exhibit a single emission band in the blue region centered at approximately 430–440 nm. This emission is attributed to excitonic recombination within the $[SnBr_6]^{2-}$ octahedra, facilitated by the confined electronic structure of the zero-dimensional hybrid framework.[22,24,26] To further investigate the electronic transitions, a photoluminescence excitation (PLE) spectrum was recorded for the powder sample (Fig. 3), with the emission fixed at 445 nm. The PLE spectrum reveals two prominent bands at 273 nm and 365 nm, corresponding to valence-to-conduction band transitions. The PL spectra of the films exhibit similar features to those of the powders but with enhanced spectral resolution and a slight blue-shift, favoured by the reduced self-absorption of the sample. This observation, together with the fact that emission does not depend on the excitation wavelength, supports its assignement to free exciton recombination (average lifetime of 0.66 ns, see Fig. S4), without
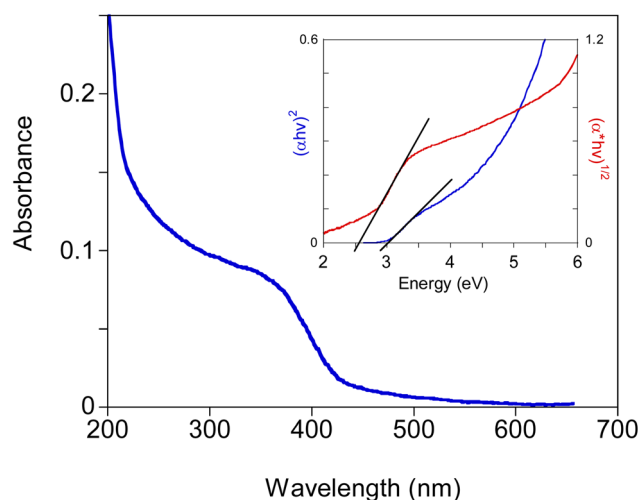

Fig. 2 UV-Vis absorption spectrum of $[Br(CH_2)_2N(CH_3)_3]_2SnBr_6$ recorded at room temperature. In the inset Tauc plots for direct (blue line) and indirect (red line) transitions.
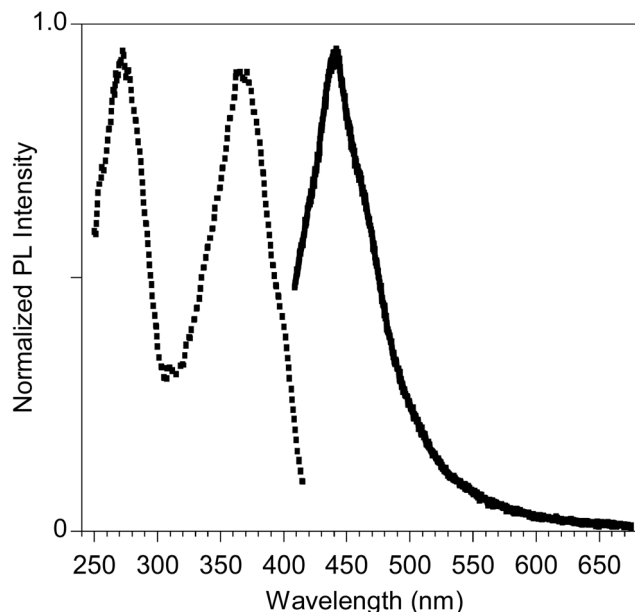
Fig. 3 PL (solid line) and PL excitation (PLE, dashed line) spectra of $[Br(CH_2)_2N(CH_3)_3]_2SnBr_6$ powder samples under 370 nm excitation, showing a peak emission at 440 nm, recorded at room temperature.

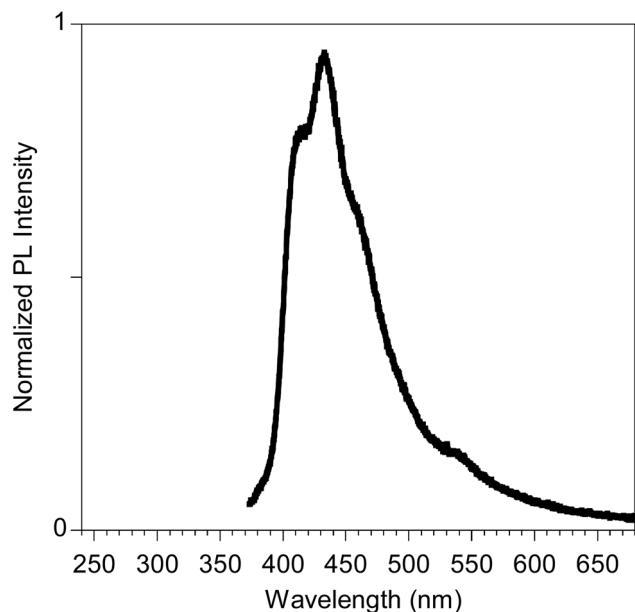**Fig. 4** Photoluminescence (PL) spectrum of $[Br(CH_2)_2N(CH_3)_3]_2SnBr_6$ cast film, under 350 nm excitation, recorded at room temperature.

contribution from emissive surface defects. The absolute Quantum Yield of the photoluminescence is below 0.1%, probably due to quenching processes induced by the material mild hygroscopic nature since all the optical characterizations were performed in ambient atmosphere. However, the sharp emission and excitonic character suggest that $[Br(CH_2)_2-N(CH_3)_3]_2SnBr_6$ may be a promising candidate for optoelectronic devices such as blue-emitting LEDs. A comparable PL response was reported for the zero-dimensional hybrid tin

halide, such as $[Cl-(CH_2)_2-NH_3]_2SnBr_{5.65}Cl_{0.35}$, which exhibits a broad emission centered around 475 nm with negligible contribution from low-energy emissive traps.[30] Such results reinforce the potential of these materials for applications in blue-emitting optoelectronic devices due to their efficient radiative recombination and structural stability.

Impedance studies

To gain deep insight into the electrical conduction process taking place in the single crystal, we carried out the complex impedance measurement at different temperatures. The complex impedance spectroscopy technique is an important tool to investigate the electrical properties of polycrystalline materials. It helps to separate the electrical resistivity due to the grain and grain boundary and provides the true picture of the electrical and dielectric properties of a material. The technique also shows the response of a system to a sinusoidal perturbation, and subsequently provides impedance as a function of
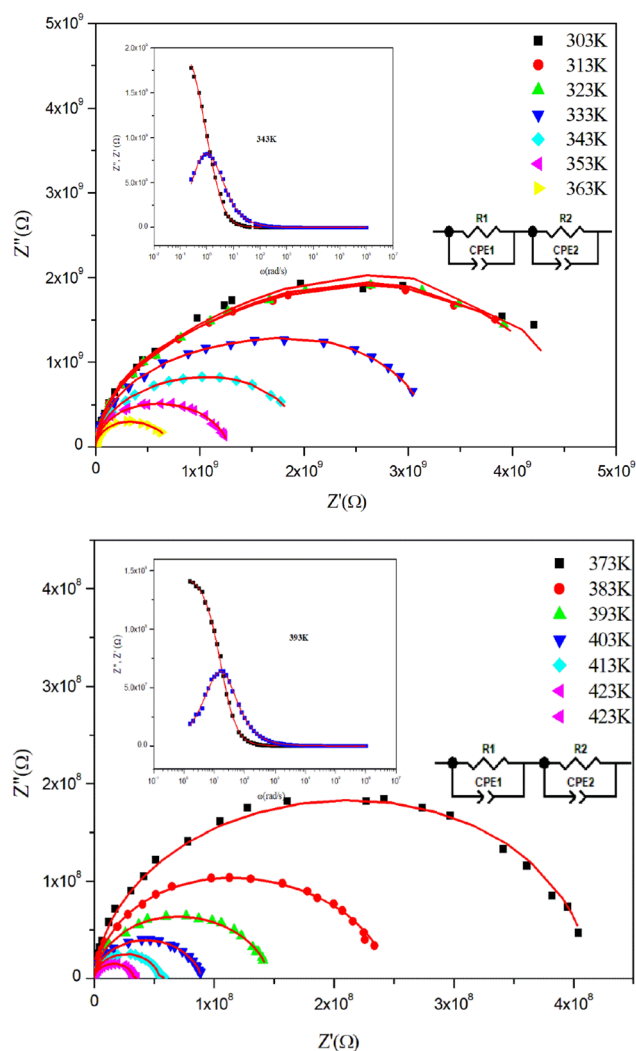

Fig. 5 Equivalent circuit, variation of Z'' and Z' plots *versus* frequencies and impedance complex plots at several temperature of the $[Br(CH_2)_2N(CH_3)_3]_2SnBr_6$ compound.

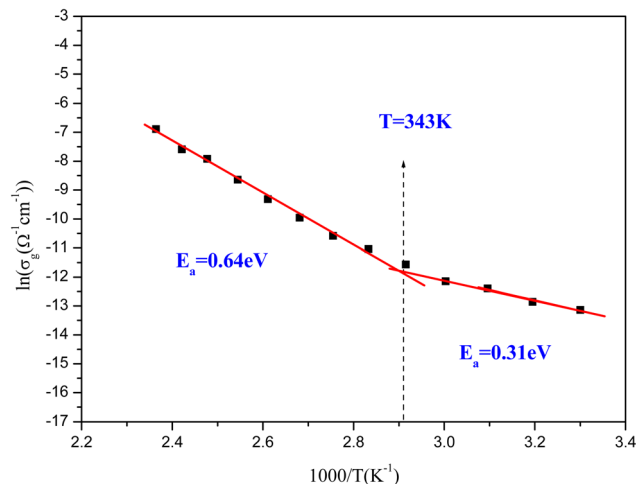**Fig. 6** Variation of Ln (σ_g) *versus* 1000/*T* of $[Br(CH_2)_2N(CH_3)_3]_2SnBr_6$.

Fig. 7 The evolution of the AC conductivity with the frequency at various temperature of $[Br(CH_2)_2N(CH_3)_3]_2SnBr_6$.

frequency. Fig. 5 shows the Nyquist plots (Z'' *vs.* Z') of $[Br(CH_2)_2N(CH_3)_3]_2SnBr_6$ materials over a temperature range of 303 K to 423 K. An asymmetrical single semicircular arc's existence for all temperatures simulated with an equivalent circuit formed by two cells in series (inset Fig. 5) shows that the material's electrical processes are contributed mainly by the interiors of the grains and grains boundary. As temperature rises, the semicircle radius decreases, indicating that sample resistance reduces, and the conductivity enhances suggesting the semiconductor character. At high frequencies the value of Z' and Z'' (inset Fig. 5) merged to the very low values. This decrease is explained by the increase of the AC conductivity in this range which is enhanced by the decrease of the disorder.[41,42] The conductivity of the grain calculated from the obtained fitted value of resistivity by the equivalent circuit is presented as a function of the inverse of the temperature in Fig. 6. More specifically, as the temperature increases, an elevated number of carriers are excited, leading thus to the increasing of the σ values. Besides, the conductive activation energy (E_a) can be calculated by employing the Arrhenius equation.[43,44] A change of the slope (activation energy) is detected around 343 K indicating the evaporation of H_2O which confirms the thermal result. The activation energy obtained in the two regions are 0.64 eV and 0.31 eV. These values are proved by similar materials, such as the $[Br(CH_2)_2N(CH_3)_3]_2CoBr_6$ with the same organic cation where the activation energy is 0.43 eV and 0.12 eV[45] which highlights the influence of Sn/Co substitution and the associated symmetrical modification on the conduction mechanism of the material.

AC conductivity

Using the real and the imaginary parts of the complex impedance data, the AC electrical conductivity was calculated as function of frequencies with various temperatures and shows in Fig. 7. In the higher frequency domain, AC conductivity increases linearly with frequency, whereas at low frequencies it is almost independent with frequency, which could be attribute to the DC contribution. Thus, DC conductivity at low
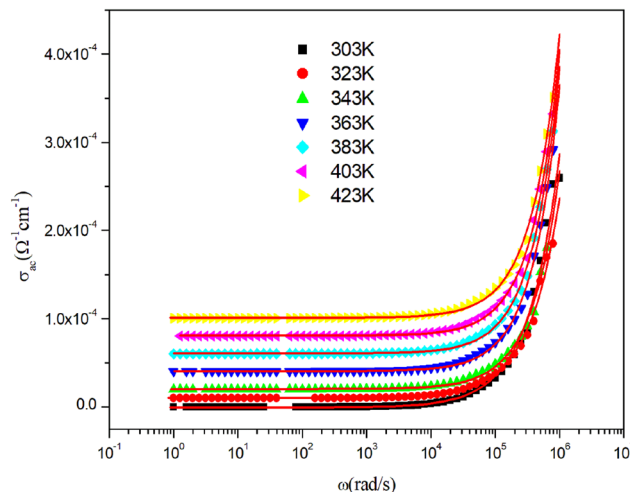
frequencies increases with increasing temperature suggesting that this last is thermally activated. To determine the value of the DC conductivities and the exponent (S) for the attribution of conduction mechanisms, these spectra are analyzed by the Jonscher power low.[46] The obtained values of DC conductivities follow this last as function of temperature as shown in Fig. 8. This variation is described by Arrhenius relation which allows to calculate the activation energy where is equal to 0.38 eV.

The values of the exponent S are inferior to 1 which indicates that the electron jump is related to a displacement with a sudden jump.[47] The variation of the exponent (S) displayed in the Fig. 9 shows two conduction mechanisms after and about the anomaly observed at 343 K in the thermal study. According to Elliot theory, the first region at low temperature is described by the NSPT model (Non-overlapping Small Polaron Tunneling), then in the second region the CBH (Correlated Barrier Hopping) is the most appropriate model to describe the conduction. In
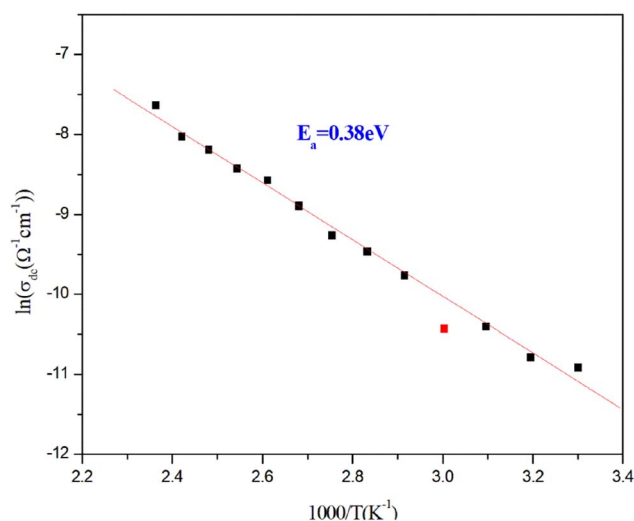

Fig. 8 Variation of Ln (σ_{dc}) *versus* 1000/*T* of $[Br(CH_2)_2N(CH_3)_3]_2SnBr_6$.

Fig. 9 The variation of *s* as a function of temperature of $[Br(CH_2)_2N(CH_3)_3]_2SnBr_6$.

Fig. 11 Variation of the Ln (ω_{max}) with reciprocal temperature of $[Br(CH_2)_2N(CH_3)_3]_2SnBr_6$.

the material studied, conduction is governed by two mechanisms depending on the conditions: NSPT (Non-overlapping Small Polaron Tunneling) and CBH (Correlated Barrier Hopping). NSPT, dominant at low temperatures, limits carrier mobility and electrical performance but ensures thermal stability and low dielectric losses. In contrast, CBH prevails at higher temperatures, enabling more efficient charge transport and enhancing device response under real operating conditions, though at the cost of increased dielectric losses. Overall, NSPT provides stable but limited conduction, while CBH enhances performance with a trade-off in energy efficiency.

Modulus studies

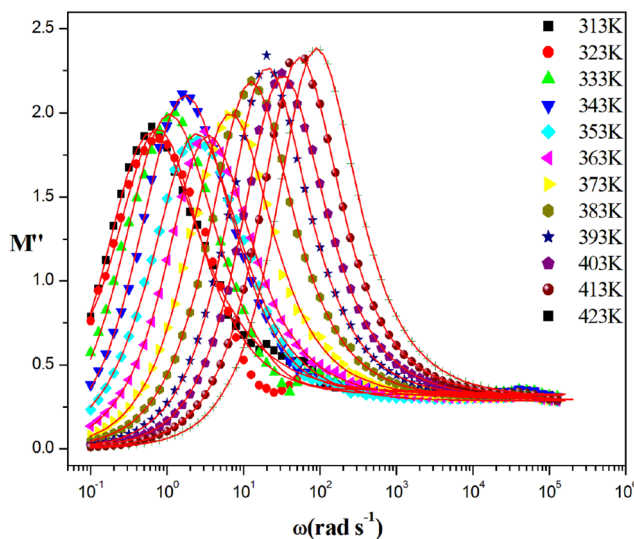The complex impedance spectrum gives more emphasis to elements with the larger resistance whereas complex dielectric

Fig. 10 The variation of the imaginary part of the electrical modulus as a function of the frequencies of $[Br(CH_2)_2N(CH_3)_3]_2SnBr_6$ at different temperatures.
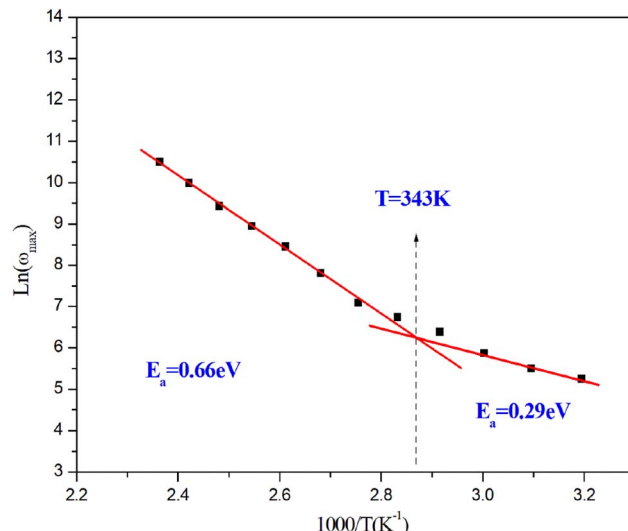
modulus plots highlight those with smaller capacitance. The complex dielectric modulus formalism, the inhomogeneous nature of the polycrystalline sample can be probed into bulk and grain boundary effects, which may not be distinguished from complex impedance plots (Cole–Cole plot). Fig. 10 displays the imaginary part of the modulus complex *versus* frequencies at various temperatures. The values of M'' are very low at lower frequency which is due to the neglect of electrode polarization.[48] A single relaxation peak in the modulus M'' spectra related with the grain and shifted to the higher frequencies with the increasing temperature. This peak is asymmetric suggesting that the conduction mechanism is linked to non-Debye type.[49] Consequently, we employed the Bergman equation[50] in the adjustment of all spectra of M'' to determinate the relaxation frequency for all temperature measurements. Fig. 11 displays the variation of the logarithm of the frequency relaxation of the grain *versus* the inverse of the temperature. This variation is described by the Arrhenius power low and indicate a change of the slope at the 343 K which confirms the thermal study and the variation of the conductivity of the grain. The activation energies in the two regions are $E_a = 0.66$ eV and $E_a = 0.29$ eV. These values are the same as those found in the variation of σ_g.

Conclusion

In summary, we have successfully synthesized and characterized a (2-bromoethyl)trimethylammonium tin(IV) bromide hybrid with 0D structure at the molecular level. The crystal structure contains one organic $[Br(CH_2)_2N(CH_3)_3]^+$ cation and an inorganic $[SnBr_6]^{2-}$ anion. The compound crystallizes in the orthorhombic space group *Pbca*, and its structural integrity is supported by a network of hydrogen and halogen bonding interactions. Optical studies reveal a direct band gap of 3.0 eV and blue photoluminescence centered at 434 nm, attributed to excitonic recombination within the discrete Sn–Br units. Thermal and electrical analyses confirm the material stability

up to 450 K and its semiconducting behavior, governed by thermally activated charge transport mechanisms. These results underline the potential of halogen-functionalized organic cations in engineering efficient, stable, and lead-free blue-emitting materials. This study contributes valuable insights toward the development of environmentally benign optoelectronic devices based on tin(IV) halides hybrids.

Author contributions

The manuscript was written through contributions of all authors. All authors have given approval to the final version of the manuscript. Amal Elghoul: conceptualization, methodology, investigation, data Curation, writing – original draft, review & editing. Bochra Ben Salah: conceptualization, methodology, investigation, data curation, supervision, writing – original draft. Fadhel Hajlaoui: conceptualization, methodology, investigation, data Curation, supervision, writing – original draft, review & editing. Karim Karoui: methodology, investigation, data curation, supervision, writing – original draft, review & editing. Nathalie Audebrand: investigation, data curation, writing – review & editing. Thierry Roisnel: investigation, data curation, writing – review & editing. Erika Kozma: investigation, data curation, writing – review & editing. Chiara Botta: investigation, data curation, writing – review & editing, funding acquisition. Nabil Zouari: investigation, data curation, writing – review & editing, funding acquisition.

Conflicts of interest

There are no conflicts to declare.

Data availability

The raw/processed data required to reproduce these findings are available and can be sent if requested.

CCDC 2474595 contains the supplementary crystallographic data for this paper.[51]

Supplementary information is available. See DOI: https://doi.org/10.1039/d5ra06415e.

Acknowledgements

References

1 A. Kojima, K. Teshima, Y. Shirai and T. Miyasaka, Organometal Halide Perovskites as Visible-Light Sensitizers for Photovoltaic Cells, *J. Am. Chem. Soc.*, 2009, **131**(17), 6050–6051, DOI: **10.1021/ja809598r**.

2 M. A. Green, E. D. Dunlop, J. Hohl-Ebinger, M. Yoshita, N. Kopidakis and A. W. Y. Ho-Baillie, Solar cell efficiency tables (Version 55), *Prog. Photovolt. Res. Appl.*, 2020, **28**, 3–15, DOI: **10.1002/pip.3228**.

3 H. J. Snaith, Perovskites: The Emergence of a New Era for Low-Cost, High-Efficiency Solar Cells, *J. Phys. Chem. Lett.*, 2013, **4**, 3623–3630, DOI: **10.1021/jz4020162**.

4 A. Babayigit, A. Ethirajan, M. Muller and B. Conings, Toxicity of organometal halide perovskite solar cells, *Nat. Mater.*, 2016, **15**, 247–251, DOI: **10.1038/nmat4572**.

5 Z. Tan, R. S. Moghaddam, M. L. Lai, P. Docampo, R. Higler, F. Deschler, M. Price, A. Sadhanala, L. M. Pazos, D. Credgington, F. Hanusch, T. Bein, H. J. Snaith and R. H. Friend, Bright light-emitting diodes based on organometal halide perovskite, *Nat. Nanotechnol.*, 2014, **9**, 687–692, DOI: **10.1038/nnano.2014.149**.

6 L. Dou, Y. Yang, J. You, Z. Hong, W.-H. Chang, G. Li and Y. Yang, Solution-processed hybrid perovskite photodetectors with high detectivity, *Nat. Commun.*, 2014, **5**(1–6), 5404, DOI: **10.1038/ncomms6404**.

7 H. Zhu, Y. Fu, F. Meng, X. Wu, Z. Gong, Q. Ding, M. V. Gustafsson, M. T. Trinh, S. Jin and X.-Y. Zhu, Lead halide perovskite nanowire lasers with low lasing thresholds and high quality factors, *Nat. Mater.*, 2015, **14**, 636–642, DOI: **10.1038/nmat4271**.

8 H. Lin, C. Zhou, Y. Tian, T. Siegrist and B. Ma, Low-Dimensional Organometal Halide Perovskites, *ACS Energy Lett.*, 2018, **3**(1), 54–62, DOI: **10.1021/acsenergylett.7b00926**.

9 A. Mitrofanov, Y. Berencén, E. Sadrollahi, R. Boldt, D. Bodesheim, H. Weiske, F. Fabian Paulus, J. Geck, G. Cuniberti, A. Kuc and B. Voit, Molecular engineering of naphthalene spacers in low-dimensional perovskites, *J. Mater. Chem. C*, 2023, **11**, 5024–5031, DOI: **10.1039/D3TC00132F**.

10 Y. Zou, Y. Gao and Y. Liu, The role of organic spacers in 2D/3D hybrid perovskite solar cells, *Mater. Chem. Front.*, 2024, **8**, 82–103, DOI: **10.1039/D3QM00726J**.

11 E. Mahal, S. Charan Mandal and B. Pathak, Understanding the role of spacer cation in 2D layered halide perovskites to achieve stable perovskite solar cells, *Mater. Adv.*, 2022, **3**, 2464–2474, DOI: **10.1039/D1MA01135A**.

12 S. Elleuch, H. Boughzala, A. Driss and Y. Abid, A One-dimensional organic-inorganic hybrid compound [(CH₃)₂C=NHCH₂CH₂CH₃][PbI₃], *Acta Crystallogr., Sect. E*, 2007, **63**, 306–308, DOI: **10.1107/S160053680605392X**.

13 M. Saliba, T. Matsui, K. Domanski, J. Y. Seo, A. Ummadisingu, S. M. Zakeeruddin, J. P. Correa-Baena, W. R. Tress, A. Abate, A. Hagfeldt and M. Grätzel, Incorporation of rubidium cations into perovskite solar cells improves photovoltaic performance, *Science*, 2016, **354**, 206–209, DOI: **10.1126/science.aah5557**.

14 A. H. Slavney, R. W. Smaha, I. C. Smith, A. Jaffe, D. Umeyama and H. I. Karunadasa, Chemical Approaches to Addressing the Instability and Toxicity of Lead-Halide Perovskite

Absorbers, *Inorg. Chem.*, 2017, **56**, 46–55, DOI: **10.1021/acs.inorgchem.6b01336**.

15 C. Yi, T. Kim, C. Lee, J. Ahn, M. Lee, H. J. Son, Y. Ko and Y. Jun, Improving FAPbBr$_3$ Perovskite Crystal Quality *via* Additive Engineering for High Voltage Solar Cell over 1.5 V, *ACS Appl. Mater. Interfaces*, 2024, **16**, 44756–44766, DOI: **10.1021/acsami.4c07749**.

16 A. Babayigit, A. Ethirajan, M. Muller and B. Conings, Toxicity of organometal halide perovskite solar cells, *Nat. Mater.*, 2016, **15**, 247–251.

17 T. J. Macdonald, L. Lanzetta, X. Liang, D. Ding and S. A. Haque, Engineering Stable Lead-Free Tin Halide Perovskite Solar Cells: Lessons from Materials Chemistry, *Adv. Mater.*, 2023, **35**, 2206684, DOI: **10.1002/adma.202206684**.

18 Y. Zhou and Y. Zhao, Chemical stability and instability of inorganic halide perovskites, *Energy Environ. Sci.*, 2019, **12**, 1495–1511, DOI: **10.1039/C8EE03559H**.

19 Y. Dang, C. Zhong, G. Zhang, D. Ju, L. Wang, S. Xia, H. Xia and X. Tao, Crystallographic Investigations into Properties of Acentric Hybrid Perovskite Single Crystals NH(CH$_3$)$_3$SnX$_3$ (X = Cl, Br), *Chem. Mater.*, 2016, **28**(19), 6968–6974, DOI: **10.1021/acs.chemmater.6b02653**.

20 Y. Sui, W. T. Chen, S. X. Ouyang, W. Q. Wang, G. X. Zhang and D. S. Liu, A Semiconducting Organic–Inorganic Hybrid Metal Halide with Switchable Dielectric and High Phase Transition Temperature, *J. Phys. Chem. C*, 2019, **123**(14), 9364–9370, DOI: **10.1021/acs.jpcc.9b00228**.

21 (*a*) L.-J. Xu, H. Lin, S. Lee, C. Zhou, M. Worku, M. Chaaban, Q. He, A. Plaviak, X. Lin, B. Chen, M.-H. Du and B. Ma, 0D and 2D: The Cases of Phenylethylammonium Tin Bromide Hybrids, *Chem. Mater.*, 2020, **32**(11), 4692–4698, DOI: **10.1021/acs.chemmater.0c01254**; (*b*) R. I. Sánchez-Alarcón, O. E. Solís, M. C. Momblona-Rincon, T. S. Ripolles, J. P. Martínez-Pastor, R. Abargues and P. P. Boix, Chemically driven dimensionality modulation of hybrid tin(ii) halide perovskite microcrystals, *J. Mater. Chem. C*, 2024, **12**, 7605–7614, DOI: **10.1039/D4TC00623B**.

22 (*a*) B. Su, G. Song, M. S. Molokeev, Z. Lin and Z. Xia, Synthesis, Crystal Structure and Green Luminescence in Zero-Dimensional Tin Halide (C$_8$H$_{14}$N$_2$)$_2$SnBr$_6$, *Inorg. Chem.*, 2020, **59**, 9962–9968, DOI: **10.1021/acs.inorgchem.0c01103**; (*b*) S. Sun, M. Lu, X. Gao, Z. Shi, X. Bai, W. W. Yu and Y. Zhang, 0D Perovskites: Unique Properties, Synthesis, and Their Applications, *Adv. Sci.*, 2021, **8**(1–23), 2102689, DOI: **10.1002/advs.202102689**; (*c*) G. Teri, H.-F. Ni, Q.-F. Luo, X.-P. Wang, J.-Q. Wang, D.-W. Fu and Q. Guo, Tin-based organic–inorganic metal halides with a reversible phase transition and thermochromic response, *Mater. Chem. Front.*, 2023, **7**, 2235–2240, DOI: **10.1039/D3QM00105A**.

23 L. Saidi, A. Samet, T. Dammak, S. Pillet and Y. Abid, Down and up conversion luminescence of the lead-free organic metal halide material: (C$_9$H$_8$NO)$_2$SnCl$_6$·2H$_2$O, *Phys. Chem. Chem. Phys.*, 2021, **23**, 15574–15581, DOI: **10.1039/D1CP01702K**.

24 (*a*) C. Zhou, Y. Tian, M. Wang, A. Rose, T. Besara, N. K. Doyle, Z. Yuan, J. C. Wang, R. Clark, Y. Hu, T. Siegrist, S. Lin and B. Ma, Low-Dimensional Organic Tin Bromide Perovskites and Their Photoinduced Structural Transformation, *Angew. Chem., Int. Ed.*, 2017, **56**, 9018–9022, DOI: **10.1002/anie.201702825**; (*b*) Z. Wang, Y. Tai, J. Nam and Y. Yin, Calcination-Induced Transformation of ZnS: Mn^{2+} Nanorods to Microparticles for Enhanced Mechanoluminescence, *Chem. Mater.*, 2023, **35**, 6845–6852, DOI: **10.1021/acs.chemmater.3c01136**.

25 H. Peng, Q. Liu, Y. Liu, Y. Lu and W. Liao, A chiral lead-free tin(iv)-based halide organic-inorganic semiconductor with dielectric switching and phase transition, *Chin. Chem. Lett.*, 2023, **34**, 107980, DOI: **10.1016/j.cclet.2022.107980**.

26 (*a*) C. Zhou, Y. Tian, Z. Yuan, H. Lin, B. Chen, R. Clark, T. Dilbeck, Y. Zhou, J. Hurley, J. Neu, T. Besara, T. Siegrist, P. Djurovich and B. Ma, Highly Efficient Broadband Yellow Phosphor Based on Zero-Dimensional Tin Mixed-Halide Perovskite, *ACS Appl. Mater. Interfaces*, 2017, **9**, 44579–44583, DOI: **10.1021/acsami.7b12862**; (*b*) G. Song, M. Li, Y. Yang, F. Liang, Q. Huang, X. Liu, P. Gong, Z. Xia and Z. Lin, Lead-Free Tin (IV)-Based Organic–Inorganic Metal Halide Hybrids with Excellent Stability and Blue-Broadband Emission, *J. Phys. Chem. Lett.*, 2020, **11**(5), 1808–1813, DOI: **10.1021/acs.jpclett.0c00096**.

27 (*a*) G.-P. Li, S.-Q. Lu, X. Chen, W.-Q. Liao, Y.-Y. Tang and R.-G. Xiong, A Three-Dimensional M$_3$AB-Type Hybrid Organic–Inorganic Antiperovskite Ferroelectric: [C$_3$H$_7$FN]$_3$[SnCl$_6$]Cl, *Chem.–Eur. J.*, 2019, **25**, 16625–16629, DOI: **10.1002/chem.201903678**; (*b*) L. Zhao, X. Han, Y. Zheng, M.-H. Yu and J. Xu, Tin-Based Chiral Perovskites with Second-Order Nonlinear Optical Properties, *Adv. Photonics Res.*, 2021, **2**(1–7), 2100056, DOI: **10.1002/adpr.202100056**.

28 J. Berger, I. Poli, E. Aktas, S. Martani, D. Meggiolaro, L. Gregori, M. D. Albaqami, A. Abate, F. De Angelis and A. Petrozza, How Halide Alloying Influences the Optoelectronic Quality in Tin-Halide Perovskite Solar Absorbers, *ACS Energy Lett.*, 2023, **8**, 3876–3882, DOI: **10.1021/acsenergylett.3c01241**.

29 H. F. Zarick, N. Soetan, W. R. Erwin and R. Bardhan, Mixed halide hybrid perovskites: a paradigm shift in photovoltaics, *J. Mater. Chem. A*, 2018, **6**, 5507–5537, DOI: **10.1039/C7TA09122B**.

30 A. Elghoul, F. Hajlaoui, K. Karoui, M. Allain, N. Mercier, E. Kozma, C. Botta and N. Zouari, Crystal structure, semiconducting and photoluminescence (PL) properties of hybrid tin perovskite-like materials: [Cl–(CH$_2$)–NH$_3$]$_2$SnCl$_6$ and [Cl–(CH$_2$)$_2$–NH$_3$]$_2$SnBr$_{5.65}$Cl$_{0.35}$, *New J. Chem.*, 2024, **48**, 12235–12245, DOI: **10.1039/D4NJ01858C**.

31 (*a*) Y. Sui, D.-S. Liu, W.-T. Chen, L.-J. Wang, Y.-X. Ma, H.-Q. Lai, Y.-W. Zhou and H.-R. Wen, Organic–inorganic Hybrid ([BrCH$_2$CH$_2$N(CH$_3$)$_3$]$_2$[CdBr$_4$]) with Unusual Ferroelectric and Switchable Dielectric Bifunctional Properties over Different Temperature Range, *Chem.–Asian J.*, 2020, **15**, 1–7, DOI: **10.1002/asia.202000241**; (*b*) Y. Sui, Y.-S. Zhong, J.-J. Wang, Q. Xia, L.-J. Wang and D.-S. Liu, A

semiconducting organic–inorganic hybrid ([$BrCH_2CH_2N(CH_3)_3$]$^{2+}$[$CuBr_4$]$^{2-}$) with switchable dielectric properties derived from an unusual piston-like displacive movement, *J. Mater. Chem. C*, 2019, **7**, 14294–14300, DOI: **10.1039/C9TC05328J**.

32 G. M. Sheldrick, SHELXT – Integrated space-group and crystal-structure determination, *Acta Crystallogr., Sect. A*, 2015, **71**, 3–8, DOI: **10.1107/S2053273314026370**.

33 G. M. Sheldrick, Crystal Structure Refinement with SHELXL, *Acta Crystallogr., Sect. C*, 2015, **71**, 3–8, DOI: **10.1107/S2053229614024218**.

34 L. Farrugia, WinGX and ORTEP for Windows: an update, *J. Appl. Crystallogr.*, 2012, **45**, 849–854, DOI: **10.1107/S0021889812029111**.

35 K. Brandenburg and M. Berndt, *Diamond (Version 2), Crystal Impact*, Bonn, 2001.

36 J. Moreau, U. Giovanella, J.-P. Bombenger, W. Porzio, V. Vohra, L. Spadacini, G. Di Silvestro, L. Barba, G. Arrighetti, S. Destri, M. Pasini, M. Saba, F. Quochi, A. Mura, G. Bongiovanni, M. Fiorini, M. Uslenghi and C. Botta, Highly Emissive Nanostructured Thin Films of Organic Host–Guests for Energy Conversion, *ChemPhysChem*, 2009, **10**, 647–653, DOI: **10.1002/cphc.200800682**.

37 X. Liu, Y. Li, T. Liang and J. Fan, Role of Polyhedron Unit in Distinct Photophysics of Zero-Dimensional Organic–Inorganic Hybrid Tin Halide Compounds, *Phys. Chem. Lett.*, 2021, **12**(24), 5765–5773, DOI: **10.1021/acs.jpclett.1c01540**.

38 C. Zhou, H. Lin, Y. Tian, Z. Yuan, R. Clark, B. Chen, L. J. van de Burgt, J. C. Wang, Y. Zhou, K. Hanson, Q. J. Meisner, J. Neu, T. Besara, T. Siegrist, E. Lambers, P. Djurovich and B. Ma, Luminescent zero-dimensional organic metal halide hybrids with near-unity quantum efficiency, *Chem. Sci.*, 2018, **9**, 586–593, DOI: **10.1039/C7SC04539E**.

39 D. Bhattacharyya, S. Chaudhuri and A. Pal, Bandgap and optical transitions in thin films from reflectance measurements, Bandgap and optical transitions in thin films from reflectance measurements, *Vacuum*, 1992, **43**, 313–316, DOI: **10.1016/0042-207X(92)90163-Q**.

40 F. Wang, H. Xie, Q. Zhao, Y. Wang, L. Meng and H. Liu, Micromechanical chemical synthesis of two tin-based organic-inorganic hybrid perovskites for high color rendering index solid-state lighting, *Opt. Mater.*, 2024, **152**, 115563, DOI: **10.1016/j.optmat.2024.115563**.

41 I. Pal, A. Agarwal, S. Sanghi, A. Shearan and N. Ahlawat, Conductivity and dielectric relaxation in sodium borosulfate glasses, *J. Alloys Compd.*, 2009, **472**, 40–47, DOI: **10.1016/j.jallcom.2008.05.022**.

42 J. C. Dyre, The random free-energy barrier model for ac conduction in disordered solids, *J. Appl. Phys.*, 1988, **64**, 2456–2468, DOI: **10.1063/1.341681**.

43 P. Zhao, B. Tang, Z. Fang, F. Si, C. Yang, G. Liu and S. Zhang, Structure, dielectric and relaxor properties of $Sr_{0.7}Bi_{0.2}TiO_3K_{0.5}Bi_{0.5}TiO_3$ lead-free ceramics for energy storage applications, *J. Materiomics.*, 2021, **7**, 195–207, DOI: **10.1016/j.jmat.2020.07.009**.

44 P. Zhao, Z. Fang, X. Zhang, J. Chen, Y. Shen, X. Zhang, Q. An, C. Yang, X. Gao, S. Zhang and B. Tang, Aliovalent Doping Engineering for A- and B-Sites with Multiple Regulatory Mechanisms: A Strategy to Improve Energy Storage Properties of Sr0.7Bi0.2TiO3-Based Lead-Free Relaxor Ferroelectric Ceramics, *ACS Appl. Mater. Interfaces*, 2021, **13**, 24833–24855, DOI: **10.1021/acsami.1c04274**.

45 I. Dakhlaoui, K. Karoui, F. Hajlaoui, N. Audebrand, T. Roisnel and F. Jomni, [$(CH_3)_3N(CH_2)_2Br$]$_2$[$CoBr_4$] halogenometallate complex: crystal structure, high-temperature reversible phase transition, electrical and optical properties, *J. Mol. Struct.*, 2021, **1231**, 129684, DOI: **10.1016/j.molstruc.2020.129684**.

46 A. K. Jonscher, Analysis of the alternating current properties of ionic conductors, *J. Mater. Sci.*, 1978, **13**, 553–562, DOI: **10.1007/BF00541805**.

47 K. Funke, Jump relaxation in solid electrolytes, *Prog. Solid State Chem.*, 1993, **22**, 111–195, DOI: **10.1016/0079-6786(93)90002-9**.

48 F. S. Howell, R. A. Bose, P. B. Macedo and C. T. Moynihan, Electrical relaxation in a glass-forming molten salt, *J. Phys. Chem.*, 1974, **78**, 639–648, DOI: **10.1021/j100599a016**.

49 A. Chen, Y. Zhi and L. E. Cross, Oxygen-vacancy-related low-frequency dielectric relaxation and electrical conduction in Bi:SrTiO₃, *Phys. Rev. B:Condens. Matter Mater. Phys.*, 2000, **62**, 228–236, DOI: **10.1103/PhysRevB.62.228**.

50 R. Bergman, General Susceptibility Functions for Relaxations in Disordered Systems, *J. Appl. Phys.*, 2000, **88**, 1356–1363, DOI: **10.1063/1.373824**.

51 CCDC 2474595: Experimental Crystal Structure Determination, 2025, DOI: **10.5517/ccdc.csd.cc2p20ng**.